



Contents list available at IJRED website

International Journal of Renewable Energy Development

Journal homepage: <https://ijred.undip.ac.id>



Research Article

Statistical Analysis on The Near-Wake Region of RANS Turbulence Closure Models for Vertical Axis Tidal Turbine

Muhammad Wafiuddin Abd Rahim^a, Anas Abdul Rahman^{a*}, Ayu Abdul-Rahman^b, Muhammad Izham Ismail^c, Mohd Shukry Abdul Majid^a, Nasrul Amri Mohd Amin^a

^aFaculty of Mechanical Engineering & Technology, Universiti Malaysia Perlis (UniMAP), Pauh Putra Main Campus, 02600 Arau, Perlis, Malaysia

^bDepartment of Mathematics and Statistics, School of Quantitative Sciences, Universiti Utara Malaysia, 06010 UUM, Sintok, Kedah, Malaysia

^cInstitute of Engineering Mathematics, Universiti Malaysia Perlis (UniMAP), Pauh Putra Main Campus, 02600 Arau, Perlis, Malaysia

Abstract. The flow field in the near wake region (up to six turbine diameters downstream) of a tidal current turbine is strongly driven by the combined wake of the device support structure and the rotor. Accurate characterisation of the near-wake region is important, but it is dominated by highly turbulent, slow-moving fluid. At present, limited number of researches has been undertaken into the characterisation of the near-wake region for a Vertical Axis Tidal Turbine (VATT) device using the Reynolds Averaged Navier Stokes (RANS) model in the shallow water environment of Malaysia. This paper presents a comprehensive statistical analysis using the Mean Absolute Error (MEA), Mean Squared Error (MSE) and Root Mean Squared Error (RMSE) on the near-wake region for shallow water application by comparing numerical solutions (i.e., different types of RANS turbulence models using Ansys Fluent) with published experimental data. Seven RANS turbulence models with a single VATT, represented by using a cylindrical object, were employed in the preliminary study. The statistical analysis performed in this study is essential in exploring and giving a detailed understanding on the most suitable RANS turbulence model to be improved, specifically on its near-wake region. In this study, the near wake region is defined as $D \leq 6$, where D is the device diameter. The analysis shows that the RANS numerical solutions are unable to accurately replicate the near-wake region based on large statistical errors computed. The average RMSE of near-wake region at $z/D = [2, 3, 4, 6]$ are 0.5864, 0.4127, 0.4344 and 0.3577 while the average RMSE at far-wake region $z/D = [8, 12]$ are 0.2269 and 0.1590, where z is the distance from the cylindrical object along the length of domain. The statistical error values are found to decrease with increasing downstream distance from a cylindrical object. Notably, the standard $k-\epsilon$ and realizable $k-\epsilon$ models are the two best turbulent models representing the near-wake region in RANS modelling, yielding the lowest statistical errors (RMSE at $z/D = [2, 3, 4, 6]$ are 0.5666, 0.4020, 0.4113 and 0.3455) among the tested parameters.

Keywords: Near-wake recovery, Grid sensitivity study, Malaysian marine energy, Error analysis, Velocity profile



@ The author(s). Published by CBIORE. This is an open access article under the CC BY-SA license (<http://creativecommons.org/licenses/by-sa/4.0/>).

Received: 18th August 2022; Revised: 6th Oct 2022; Accepted: 30th Oct 2022; Available online: 11th Nov 2022

1. Introduction

Research and development on tidal stream energy in Malaysia are still in preliminary stage compared to other renewable energy sources because this sector has not received adequate attention from the local government (Samo *et al.*, 2020; Yaakob, Yasser, *et al.*, 2013). Since most Research and Development (R&D) financing in Malaysia is provided by the government, this has slowed down the development of local tidal stream energy particularly in the matter of resources, environmental impacts, technology commercialisation, human capital, and skills development (Cetina-Quiñones *et al.*, 2021; Economic Planning Unit, 2015; Mohd Chachuli *et al.*, 2021; Petinrin & Shaaban, 2015). The official legislators and decision-makers must be apprised that the scarce R&D resources should be used properly while available. This is to ensure that the renewable energy policy goals can be met with the funding allocation and assets on hand. At present, Malaysian academic institutions, particularly universities, are continuously engaging in marine energy research by actively working on establishing research

facilities intended for device deployment in the Malaysian shallow water environment. Crucially, two issues must be addressed before any device can be deployed into the waters (i) device potential and ability to harness energy from the slow-moving flow environment and (ii) technology readiness level for most of the devices, which is still in the infancy stage (Behrouzi *et al.*, 2014; Elbatran *et al.*, 2016; Hassanzadeh *et al.*, 2018; Husain *et al.*, 2019; Kai *et al.*, 2021; Yaakob *et al.*, 2018; Yaakob, Suprayogi, *et al.*, 2013).

Harnessing tidal stream energy in shallow water environments is highly dependent on tidal stream velocity and water depth for cost-effective power generation. In particular, the average tidal stream velocity in the shallow water of Malaysia is approximately 1.0 m/s (Ghazvinei *et al.*, 2018; Rahman *et al.*, 2019; Salem *et al.*, 2015). This velocity is significantly lower than the minimum flow speed required for the horizontal axis tidal turbine (HATT), but it is appropriate for vertical axis tidal turbine (VATT) deployment (Abdullah *et al.*, 2021; Bonar *et al.*, 2018; Elbatran *et al.*, 2018; Lafleur *et al.*, 2020). Nevertheless, there are areas experiencing high marine current

* Corresponding author
Email: anasrahman@unimap.edu.my (A. A. Rahman)

flows which include narrow straits, between islands, around the headland, and entrance to lochs, bays, and large harbours where the average tidal stream velocity is between 1.0 m/s to 1.5 m/s with high potential for tidal stream energy extraction (Bonar *et al.*, 2018; Ghazvinei *et al.*, 2018; Lee & Seng, 2009; Lim & Koh, 2010; Rahman *et al.*, 2019; Salem *et al.*, 2015). Besides, water depth at areas experiencing high marine current flows in Malaysia is considered shallow, with an average depth of 30.0 m (Garces *et al.*, 2006; Sakmani *et al.*, 2013). For example, the Malacca Strait has a range of water depth between 28.75 m to 59.53 m along the east coast of the Malaysian Peninsular. The strait is wider and deeper in the northern part with an average depth of 66.0 m, but it becomes narrower and shallower towards the southern part with an average depth of 30.0 m.

Accurate wake modelling research is a crucial part in designing tidal stream turbines before making them commercially viable in the market. Both experimental laboratory studies and Computational Fluid Dynamics (CFD) modelling have led to a better understanding of wake characteristics produced by tidal stream devices (Maganga *et al.*, 2010; Mason-jones *et al.*, 2012; Myers & Bahaj, 2010; Salunkhe *et al.*, 2019; Shen, 2002; Tedds *et al.*, 2014; Vermeer *et al.*, 2003). Actuator disc (AD) approach is used as a turbine representation in harnessing tidal stream energy in some of the earliest experimental and numerical modelling studies. This method characterises turbine as a simple disc with identical dimensions to the rotor and is also utilised to represent the forces exerted on the fluid circulation (Johnson *et al.*, 2014). The AD approach has been used in several research publications to characterise tidal stream turbines' framework within a formulation of the RANS equations (Abdul Rahman, 2018; Batten *et al.*, 2013; Costa Gomes; *et al.*, 2014). The idea is to use a disc with the same shape as the turbine to simulate the forces it imparts to the surrounding flow. The RANS equations are discretised, and the forces are represented as negative momentum source terms in cells representing the rotor structure.

The movement of water circulation at downstream of a tidal stream turbine is commonly classified as follows: (1) near-wake region (up to 6D), (2) intermediate-wake region (6D to 10 D); and (3) far-wake region (beyond 10D), where D is the rotor diameter (Afgan *et al.*, 2013; Clary *et al.*, 2020; Harrison *et al.*, 2010; Maître *et al.*, 2013; Myers & Bahaj, 2010). To date, researchers have focused on the mean streamwise flow and turbulence intensity in single planes downstream of the turbine, with measurements constrained to a central plane through the motor as well as planes parallel to the water circulation. The majority of the experimental revisions conducted were mostly interested in understanding the flow characteristics at the far-wake region (Clary *et al.*, 2020; Harrison *et al.*, 2010; Maître *et al.*, 2013; Tedds *et al.*, 2014). The near-wake has certain boundaries in terms of its accuracy; though the effects of swirl were not considered, numerical modelling is one of the available approaches for evaluating the implications of the far-wake flow. As a result, turbulence closure models that presume turbulent isotropy, such as the k- ϵ , will be unable to describe the near-wake turbulence field appropriately.

Earlier numerical modelling research has commonly underestimated the near-wake turbulence primarily due to the fact of the presumption made, i.e., an isotropic turbulent flow field. However, differences in wake characteristics are less pronounced with increasing downstream distance showing that, for single devices, the ambient flow has a large influence on the far wake characteristics while the near wake is dominated by device-specific features and aerodynamic/hydrodynamic characteristics of the turbine blades. Therefore, this study aims to investigate a simulated near-wake turbulence region across

six varying downstream distances throughout the whole width of a channel downstream of a turbine, providing the most comprehensive three-dimensional velocities and turbulence statistics data set available. In achieving the aim, statistical analysis on numerical modelling of the near-wake region using various RANS turbulence closure models was carried out to investigate the accuracy and precision of the selected models with reference to experimental data obtained from literature.

2. Methodology

The AD momentum theory has been commonly employed in wind and tidal turbine simulation (Abdul Rahman, 2018; Batten *et al.*, 2013; V M M G Costa Gomes; *et al.*, 2014). Actuator cylinder model is similar to the AD model but has different axes of orientations for the turbine, as shown in Fig. 1. Both methodologies are based on one-dimensional assumption, suggesting that the difference in velocity as well as pressure across the surface of a rotor is constant. In both approaches, the turbines are assumed to be solid objects (disc and cylinder) as constant sink of momentum. These approaches are extended by the RANS AD approach, which takes into account three dimensions (considering x-y-z planes of axis), turbulence, and user-specified boundary conditions. However, this study employed a hypothetical "actuator" cylinder, where instead of calculating the negative momentum source term, physical objects in the form of a cylinder and disc were used to represent the turbines.

2.1 Hypothetical Cylindrical Approach

The term "actuator cylinder" refers to a cylindrical object that provides a continuous resistance to the incoming flow. The RANS hypothetical cylindrical approach was used to resolve the three-dimensional components of turbulence. The Reynolds-averaged equations of mass conservation is described in Equation (1) while momentum conservation is presented in Equation (2).

Mass conservation

$$\frac{\partial U_i}{\partial x_i} = 0 \quad (1)$$

Momentum conservation

$$\frac{\partial(\rho U_i)}{\partial t} + \frac{\partial(\rho U_i U_j)}{\partial x_j} = -\frac{\partial P}{\partial x_i} + \frac{\partial}{\partial x_j} \left[\mu \left(\frac{\partial U_i}{\partial x_j} + \frac{\partial U_j}{\partial x_i} \right) \right] + \frac{\partial}{\partial x_j} (-\rho \overline{u'_i u'_j}) + \rho g_i + S_i \quad (2)$$

where U_i ($i = u, v, w$) is the velocity of water averaged over time t , x_i ($i = x, y, z$) is the distance, ρ is the density of water, P is mean pressure, μ is viscosity, $-\rho \overline{u'_i u'_j}$ is the Reynolds stress which must be resolved with a turbulence model, u' is an instantaneous velocity fluctuation over time dt from the mean velocity, g_i is the component of gravitational acceleration and S_i is an added source term to the $i = x, y$ or z momentum equation.

2.2 Numerical Modelling

Numerical simulation was carried out using Ansys Fluent which solved Equations (1) and (2). This is predominantly due to its capability to offer a variety of numerical algorithms for simulating fluid dynamics problems (Batten *et al.*, 2013; Johnson *et al.*, 2014; Lavaroni *et al.*, 2014; Ren *et al.*, 2019; Salunkhe *et al.*, 2019).

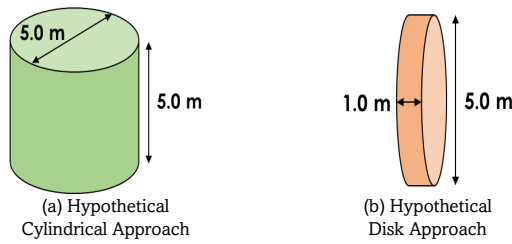


Fig. 1 Distinct axes orientation for modelling tidal stream devices: (a)Cylindrical shape to represent VATT

In this research, Ansys Fluent was utilized to solve the governing equation with two different solvers, that is pressured-based and density-based solvers. Ansys Fluent pressured-based solver has segregated and coupled algorithms. The pressure-based solver had been used to conduct stable numerical computations of RANS turbulence models. The Pressure-Implicit with Splitting of Operators (PISO) approach was used to conduct pressure-velocity coupling. A second-order implicit (three-point backward difference) approach was used to discretize unsteady terms. The convective components in the

momentum equations were discretized using a second order upwind technique for Unsteady Reynolds Averaged Navier Stokes (URANS) and the second-order bounded central difference technique for improved delayed detached eddy simulation (IDDES) and monotonically integrated LES (MILES).

2.2.1 Turbulence Models

Tidal flow simulation for the shallow water environment of Malaysia was conducted using Ansys Fluent for a few selected RANS models that are commonly used in the Ansys software package as evidenced from previously published literature (Blackmore *et al.*, 2011; Clary *et al.*, 2020; Ding *et al.*, 2020; Jump *et al.*, 2020; Salunkhe *et al.*, 2019; Shur *et al.*, 2008; Tedds *et al.*, 2014; Vinod *et al.*, 2021). Table 1 lists the selected RANS models along with their detailed descriptions. Since this numerical study was carried out for the Malaysian shallow water environment, averaged tidal stream velocity of 1.0 m/s (Ghazvinei *et al.*, 2018; Rahman *et al.*, 2019; Salem *et al.*, 2015) and averaged water depth of 30.0 m (Garces *et al.*, 2006; Sakmani *et al.*, 2013; Yaakob *et al.*, 2006) were set as controlled parameters based on available literature.

Table 1
Selected RANS turbulence models used in this study with detailed descriptions and their respective characteristics

Turbulence Models	Descriptions / Characteristics
Spalart-Allmaras	<ul style="list-style-type: none"> i. A single transport equation model that solves directly for an altered turbulent viscosity. This model is utilised in applications requiring wall-bounded flows on a fine near-wall mesh. Fluent’s implementation supports the use of low degree order of meshes (coarser refinement). The option to integrate the strain rate in the production term enhances the estimation of vortical flows. ii. Cost-effective in regard to computational requirement and processing time for big meshes. Ideal for slightly complicated (quasi-2D) external/internal flows and pressure-induced boundary layer flows.
Standard k-ε	<ul style="list-style-type: none"> i. This is a benchmark for two-transport-equation model which solve the k and ε components. This is the default for k-ε model. Coefficients are obtained empirically but are only relevant for completely turbulent flows. ii. It is a robust model. Although the model is having obvious restriction, but it is widely utilised in numerical simulation. It faces significant challenges in complicated fluid circulation that requires a high-pressure gradient, a separation, and a severe streamline curvature. It is ideal for preliminary iteration, alternative design screening and parametric investigations.
RNG k-ε	<ul style="list-style-type: none"> i. It is a divergent of the conventional k-ε model where the mathematical equation and its variables are analytically derived. Substantial adjustments to the ε equation increase the model's capacity to simulate extremely strained flows. It is an alternative assist in the prediction of whirling and low Reynolds number fluid circulation. ii. It provides most of the features and advantages as well as uses offered in Realizable. This model is more difficult to converge than Realizable
Realizable k-ε	<ul style="list-style-type: none"> i. It is another variation of the standard k-ε model. Its “realizability” originates from improvements which permit specific mathematical restrictions to be satisfied, thereby enhancing the effectiveness of the algorithm. ii. It is ideal for complicated shear flows which involves sudden strain, considerable mild swirl, vortices, and regionally transitional fluid flows
Standard k-ω	<ul style="list-style-type: none"> i. It is a two-transport-equation model (i.e., the specific dissipation rate (ε / k) of this model is developed based on Wilcox (1998) that provides a solution for k and ω components. This is the default k-ω model. It performs better than k- models for wall-bounded and low Reynolds number flows. This model has taken into account for low Reynolds number effects, free shear, and compressible flows. ii. This model is ideal for complicated boundary layer flows with an unfavourable pressure gradient and separation. Separation is expected to be extensive and premature.
SST k-ω	<ul style="list-style-type: none"> i. This is another divergent of the standard k-ω model mentioned above. Utilising a blending function, this model combines the original Wilcox model for application of near walls and the standard k-ε model away from walls. Additionally, it restricts turbulent viscosity to ensure that τ_r ~ k is maintained. ii. This model provides comparable advantages as delivered by standard k-ω model. Unlike its baseline model, SST k-ω is not excessively responsive to inlet boundary conditions. It predicts flow separation better than others accurately and precisely.
RSM	<ul style="list-style-type: none"> i. Reynolds stress equation model is directly addressed using transport equations, removing the isotropic viscosity hypothesis that is used in other models. It is utilised for extremely whirling flows. The quadratic pressure-strain alternative enhances the effectiveness for many fundamental shear flows application. ii. It is the most fundamental prospect of RANS model. The presumption of isotropic eddy viscosity is eliminated. It takes more time to solve the numerical simulation. Thus, it is more difficult to converge in simulation because of the strong connection of equations. It is ideal for complicated three-dimensional flows with high streamline curvature and vortices.

Source: ANSYS (2014), Hassanli (2019), Matus (2016)

Table 2
Input parameters for numerical modelling

Input Parameters	Value / Dimension
Diameter of Cylinder, D	5.0 m
Height of Cylinder, H	5.0 m
Blockage ratio	0.0191
Depth of domain, y	34.0 m
Width of Domain, x	34.0 m
Length of Domain, z	250.0 m
Position of Cylinder	62.5 m

2.2.2 Model dimension / simulation condition

The simulations were performed using a hypothetical cylindrical approach which is similar to the AD model, which has the most extensive empirical data that is accessible. This study is primarily focused on the comparison of various types of RANS Turbulence Models against the experimental conditions reported by (Clary *et al.*, 2020; Maître *et al.*, 2013) using statistical analysis by evaluating the Mean Absolute Error (MEA), Mean Square Error (MSE) and Root Mean Square Error (RMSE). This will be further discussed in Sections 2.5 and 2.6.

The methodology in setting up the hypothetical cylindrical approach to be used in numerical simulation was based on previous literature (Harrison *et al.* 2010; Garcés *et al.* 2006; Sakmani *et al.* 2013; Abdul Rahman 2018; Yaakob, Rashid, and Mukti 2006) as shown in Table 2. Therefore, as demonstrated in Table 2, the model domain was defined as a 62.5 m long inflow zone, with the 5.0 m diameter cylinder turbine located at the centre of a 30.0 m water column and a 187.5 m outflow. The flow was presumed to be at steady state and symmetrical, and a symmetry plane was employed to cut through the centre of the flume and disc, reducing the calculation time in half.

2.2.3 Domain and grids

The domain of the models comprised of two blocks in all simulations: a hexahedron outer block and a cylindrical blade assembly block, with the cylindrical disc positioned at the origin ($x = 0, y = 0, \text{ and } z = 0$), as illustrated in Fig. 2 and Fig. 3. The outer domain encompassed $x = [-3.4D, 3.4D], y = [-3D, 3D], \text{ and } z = [-13.5D, 36.5D]$. The cylindrical disc domain was 1D in diameter and extended from $y = [-0.5D, 0.5D]$. Unstructured, hybrid (mixed element) meshes were used in the simulations, with disc surfaces discretized using triangular or quadrilateral elements extruded normal to the wall to obtain eight layers of prismatic cells in the boundary layer, as shown in Section 2.2.4. Mixed-element unstructured cells were used away from the boundary layer.

2.2.4 Mesh independence study

The unstructured hexa-mesh was developed for each turbulence models using Ansys Fluent with 5 distinct element sizes for the domain as shown in Table 3. Additionally, mesh refinement was applied at the faces and edges of the cylindrical object (i.e., the VATT) as also shown in Table 3. The solutions used and shown in this paper were calculated based on the finest mesh. On all meshes parameters were within the limits proposed in the Ansys Fluent manual to reduce discretisation inaccuracies (Salunkhe *et al.*, 2019).

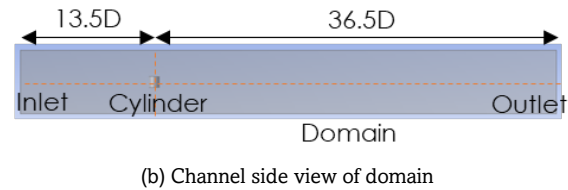
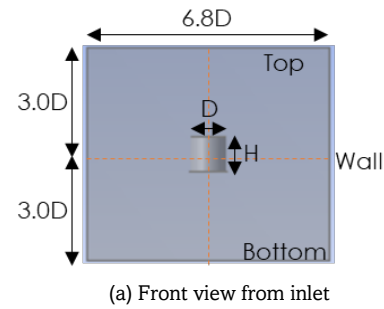


Fig. 2 Schematic diagram of cylinder and domain used in this project (front and side views)

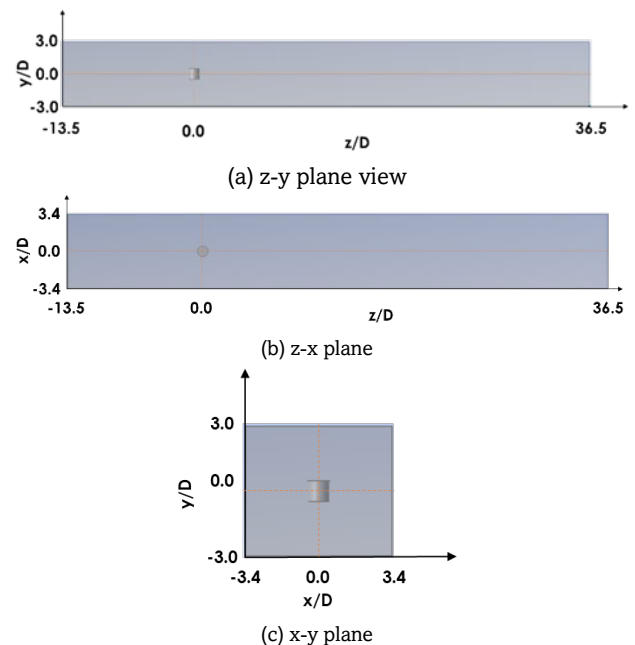


Fig. 3 Schematic diagram of cylinder and domain used in this project (z-y, z-x and x-y plane views)

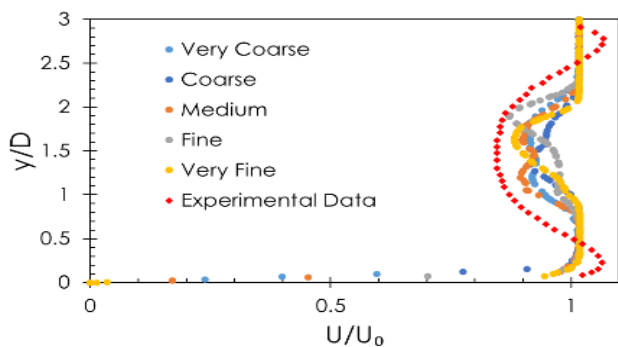
Table 3
Parameter specification for boundary condition

Type (refinement)	Element	Element size (m)	Nodes	No. of elements
1 (very coarse)	Domain	2.00	51,513	282,354
	Faces	1.00		
	Edges	1.00		
2 (coarse)	Domain	1.75	74,115	411,892
	Faces	0.80		
	Edges	0.80		
3 (medium)	Domain	1.50	114,146	636,727
	Faces	0.60		
	Edges	0.60		
4 (fine)	Domain	1.25	187,969	1,060,698
	Faces	0.40		
	Edges	0.40		
5 (very fine)	Domain	1.00	361,359	2,048,678
	Faces	0.20		
	Edges	0.20		

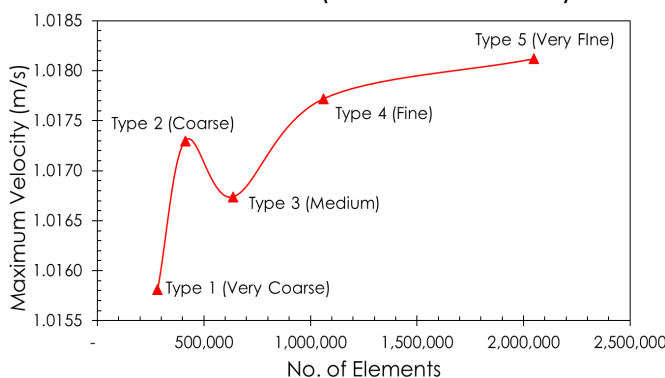
Based on Table 3, it is shown that reducing the element size of domain, faces and edges (from very coarse to very fine refinement) would increase the number of nodes and elements in the numerical simulation. This in turn would increase the quality and accuracy of the solutions of the numerical study. However, generating a high quality of mesh influences the required time for the simulations to conclude. It has been recorded that higher order of mesh generation takes the longest time for the meshing process, i.e., the process in which the continuous geometric space of domain, faces and edges is broken down into smaller shapes to properly define the physical shape of the domain, faces and edges, followed by medium and coarse mesh.

The time taken for the mesh generation to complete were 10 minutes for very fine mesh, 8 minutes for fine mesh, 6 minutes for medium mesh, 4 minutes for coarse mesh and 3 minutes for very coarse mesh. Besides, the time needed to solve the numerical simulation after setting up the boundary conditions in ANSYS Fluent is highly influenced by the quality and accuracy of the meshing. Consequently, it was concluded that detailed mesh generation took the longest time to solve the numerical solution (i.e., 41 minutes), followed by fine, medium, coarse and very coarse mesh (i.e., 25 minutes, 14 minutes, 10 minutes and 7 minutes respectively).

Velocity profiles for the grid-independent study at 12D downstream from cylindrical object are illustrated in Fig.4 (a), where the five distinct meshing refinements (as highlighted in Table 3) seems to display a similar velocity pattern against the experimental data. Though there are small deviations between the five refinement parameters, which is expected considering the variation in the number of elements between them, general profile behaviour indicates that the chosen grid refinements options are suitable to be employed for this study.



(a) Velocity profile at 12D Downstream for various grid refinement sizes



(b) Velocity profile at 12D downstream at different meshing refinement

Fig. 4 Velocity profile at 12 downstream at (a) various grid refinement size and (b) different meshing refinement

Nevertheless, further analysis on the conducted refinement reveals different perspectives in the selection of meshing refinement, as shown in Fig. 4 (b). The analysis shows that variations of meshing refinement from very coarse to very fine have significant impacts on the maximum velocity generated in numerical simulation, thus affecting velocity profile at different downstream regions. Therefore, Type 5 (i.e., very fine) meshing refinement was selected to be the ideal element size of the overall domain. This mesh size would generate the best result with considerable time for numerical calculation and analysis compared to finer mesh. Correspondingly, detailed characteristics of mesh generated from the five types of meshing refinement are depicted in Table 4 to Table 8. From these tables, the influence of mesh element sizes in creating an accurate representation of the device can be clearly observed, where smooth elements transition from the domain, faces and edges are apparent on the model utilising very fine grid sizing (Type 5).

2.2.5 Boundary conditions

A Neumann boundary condition was employed for the pressure at the inflow while the Dirichlet boundary condition was utilised for the velocity. The free surface was neglected, and the top boundary was defined by a zero-gradient slip boundary condition. The inflow, outflow, and top wall plane were established as the boundary conditions with the specifications listed in Table 9 and these were subjected to the non-slip condition. At the outflow, a fixed pressure boundary condition was applied. For the cylindrical disc, as well as the bottom and side borders, a wall-function boundary condition was adopted.

2.3 Scaling Issues

The comparison data used in this work were for a downsized setting that was constrained by the laboratory equipment’s geometry. Measurements were taken behind a 0.175 m diameter VATT (reduced-scaled Darrieus turbine) in 0.7 m of water at a uniform inlet flow rate of approximately 2.3 m/s.

Froude numbers in the range of 0.1–0.2 are acceptable for full-scale channels, while numbers below 0.5 are typically assured steady flows when there are no obstructions in the surrounding water. Critical flow conditions may arise at Froude numbers approaching one, resulting in standing waves (hydraulic leaps) and transient surface effects. Because these interactions are relatively uncommon at full-scale, Froude similarity is preserved such that the free surface at model scale changes shape in the same way as the full-scale system.

Preserving Froude similarity frequently results in substantially lower Reynolds values in the model. This is widely acknowledged, presuming the open flow regime is within the turbulent range, which would be the case for the scales employed in this study.

The magnitude of thrust exerted by the turbine on the stream is the fundamental factor for evaluating the far-wake whenever scaling the turbine (Yang *et al.*, 2021). As a result, the non-dimensional thrust components (Wang & Liu, 2021) remains constant in both numerical models and full-scale situations.

Table 4
Parameter specification for boundary condition (Type 1 – very coarse grid)

Type	Element	Mesh Generation
(Type 1 – very coarse grid)	Domain	
	Faces	
	Edges	

Table 6
Parameter specification for boundary condition (Type 3 – medium grid)

Type	Element	Mesh Generation
(Type 3 – medium grid)	Domain	
	Faces	
	Edges	

Table 5
Parameter specification for boundary condition (Type 2 – coarse grid)

Type	Element	Mesh Generation
(Type 2 – coarse grid)	Domain	
	Faces	
	Edges	

Table 7
Parameter specification for boundary condition (Type 4 –fine grid)

Type	Element	Mesh Generation
(Type 4 –fine grid)	Domain	
	Faces	
	Edges	

Table 8
Parameter specification for boundary condition (Type 5 – very fine grid)

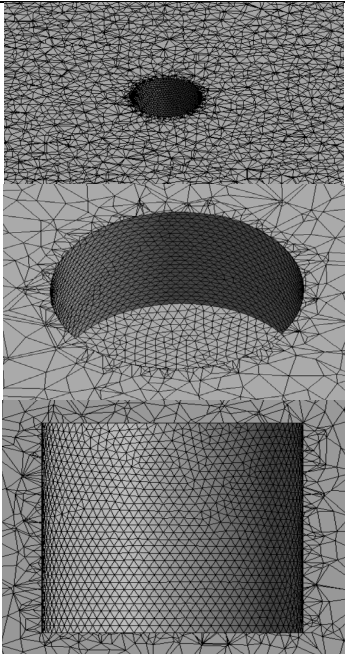
Type	Element	Mesh Generation
Type 5 – very fine grid)	Domain	
	Faces	
	Edges	

Table 9
Parameter specification for boundary condition

Type	Parameter	Specification
Fluid	Medium	: Seawater
	Temperature	: 27°C
	Density	: 1023 kg/m ³
	Dynamic viscosity	: 0.00092 kg/ms
Inlet	Inflow velocity	: 1.0 m/s
	Method	: Intensity & hydraulic diameter
	Hydraulic diameter	: 0.1 m
	Turbulence intensity	: 5%
Outlet	Method	: Intensity & hydraulic diameter
	Hydraulic diameter	: 0.1 m
Top Wall Solution	Shear condition	: Specified shear
	Method	: SIMPLE scheme
	Turbulent KE	: 2 nd order upwind
	Turbulent dissipation rate	: 2 nd order upwind

2.4 Limitations of Cylindrical Object

The effectiveness of the cylindrical object to represent Vertical Axis Tidal Turbine (VATT) is restricted by a few constraints. Most of these constraints are associated with hydrodynamic effects in the near-wake region which diminish 6D further downstream – i.e., having minimal effect on the flow further downstream (Yaakob, Yasser, *et al.*, 2013). There are several circumstances in which research on the near-wake region is unlikely to be of major interest, such as, (i) designing and simulating tidal farms; (ii) investigating free surface effects or (iii) examining environmental implications. Since wind turbines do not tend to be positioned closer than 7D apart (in general

wind turbine farm configuration), this is to be the same for the tidal farm (Yaakob, Yasser, *et al.*, 2013). Thus, despite its drawbacks, the use of cylindrical objects can still be usefully applied. The limitations of this approach are highlighted in Table 10.

2.5 Experimental Data

The validation process of the numerical simulation results was performed by comparing the experimental result published by (Clary *et al.*, 2020). In their, Particle Image Velocimetry (PIV) quantification was carried out in multiple horizontal planes of varying elevations in the experimental hydrodynamic tunnel downstream of the rotor at the Laboratoire des Ecoulements Géophysiques & Industriels (LEGI). The test section had a rectangular form (length x width x height = 1000 x 700 x 250 mm), as shown in Fig. 5.

The rotor employed in the previous experiment conducted by both Clary *et al.* and Maître *et al.* (2013) was a three-bladed reduced-scale Darrieus turbine. Fig. 5 illustrates its features. It had a D = 175 mm diameter and a H = 175 mm height. The blades had NACA0018 profiles with a camber that followed a 175 mm rotating circle. It had a chord value of c = 32 mm, resulting in a solidity of $2nc/D = 1.1$. The origin of all coordinates in this work is the intersection of the rotation axis and the mid-height plane of the turbine. The x-axis was along the inlet flow direction, z, was the vertical axis and y, the transverse axis.

The complete setup used in this experiment can be illustrated in Fig. 6. A convergent (label no 7) was placed upstream of the test section, including a Pitôt probe (label no 8) to measure the average velocity. In the test section, the velocity ranges from 1 to 2.8 m/s. The inferior and the two lateral walls were made from altuglass to allow flow visualizations. The superior wall (label no 9) was made from aluminum in order to support the experimental apparatus. The measurement platform (label no 10) was mounted on the top of the test section by means of four rigid cylindrical supports (label no 11).

Table 10
Limitations of cylindrical object in comparison to full turbine model to harness tidal stream energy

No.	Limitations
1	Energy extraction is incompatible for both scenarios – i.e., AD and hypothetical cylindrical object. The numerical simulation computationally removes the momentum, leading to a lower downstream velocity. However, cylinder object in the experiment extracts from water circulation by transforming momentum of streamwise into small-scale turbulent structures, that disintegrate immediately behind the rotor;
2	The blades of a revolving rotor generate tip vortices. These vortices will not be generated in experiment or model;
3	Unlike revolving blades, the cylinder object does not revolve and hence does not generate any swirl into the stream. The hypothetical cylindrical method assumes that, further than the near-wake region, the stream will have a similar structure to that of a rotor (i.e., most swirl elements dispersed together with the disc induced turbulence). The downstream limit of the near-wake is described as the point where the shear layer (which forms between the wake's border and the free stream flow) approaches the wake centre-line; and
4	The hypothetical cylindrical technique does not take into consideration of transient flow characteristics. It contains data on mean flow characteristics and isotropic turbulence. As a result, the model may be used to better understand the fundamental properties of the flow behind the turbine.

Source: Harrison *et al.* (2010); Clary *et al.* (2020)

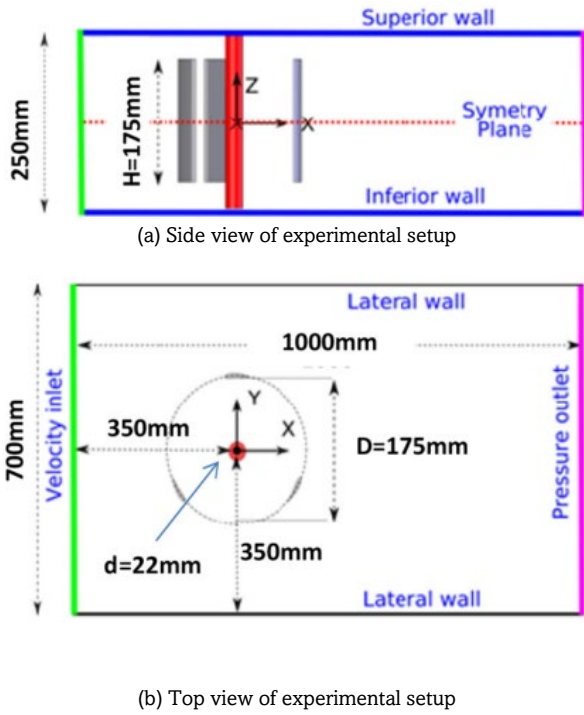


Fig. 5 Schematic diagram of experimental setup used as a reference, (a) side and (b) top views (Maitre et al., 2013)

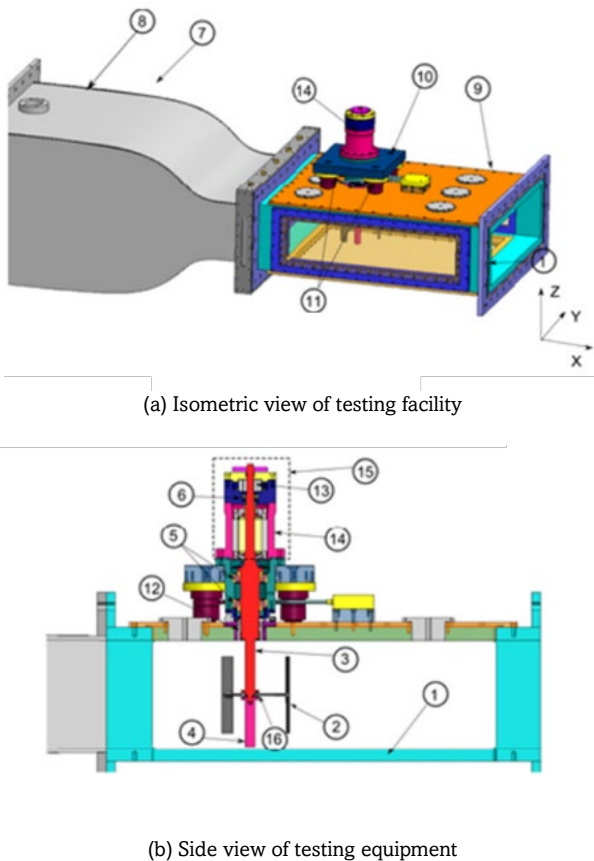


Fig. 6 Complete experimental setup used to measure the velocity profile at different downstream (Clary et al., 2020; Maitre et al., 2013)

The torque was measured via a frameless permanent magnet servomotor kit (label no 15) mounted above the platform. It includes an electrical synchronous generator (label no 14) used to drive the turbine at the desired rotational speed: A proportional-integral regulation was used to impose a constant rotation speed by controlling the electric current and consequently the instantaneous torque applied on the turbine. The PI parameters were chosen to avoid high pick torques that could damage the structure of the turbine, particularly at the hub blade attachments.

Consequently, the rotational speed fluctuates slightly around the imposed value. The angular position and the rotational speed were given by the resolver (label no 13). The rotating shaft (label no 3) were placed from the mid-height test section, and through the electrical generator rotor and slightly exceeded the servomotor kit. The blades (label no 2) were attached to the hub (label no 16) via horizontal arms. The shaft was prolonged below the hub using a polymer material (label no 4) to realize the symmetry plane at the turbine centre. The shaft was guided by a pair of ball bearings (label no 5), between the superior wall (label no 9) and the platform (label no 10) and by another ball bearing (label no 6), between the generator and the resolver housings. A lip type sealing system (label no 12), between the turbine rotating shaft and the superior wall, were used to prevent water leakage.

2.6 Statistical Analysis

Since the number of numerical data points obtained from the model is much larger than the experimental data points, a trendline was applied to the velocity profile of the experimental curve. Fig. 7 provides an overview of the generated polynomial trendline on the velocity profile at 2D downstream of the cylindrical object. Firstly, the polynomial trendline option was imposed on the extracted experimental data. Then, the polynomial order was set to the highest value (n = 6) to ensure the resulted R-squared (R²) value approaches 1, where R² = 1 indicates a perfect fit. The equation of the polynomial trendline was then used to plot a new curve using each data set from the employed RANS turbulence models.

The difference between predicted (data set of new experimental curve from the generated polynomial trendline) and observed (data set from the simulation using various RANS turbulence models) values can be evaluated using Mean Absolute Error (MEA), Mean Squared Error (MSE) and Root Mean Squared Error (RMSE), where the smallest value among models being evaluated indicates the best model performance. The MEA, MSE, and RMSE can be computed as follows:

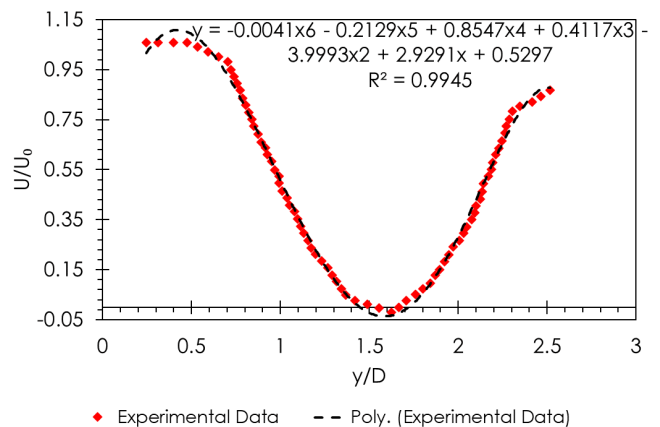


Fig. 7 Imposed trendline on the velocity profile at 2D downstream of cylindrical object

$$MEA = \frac{1}{n} \sum_{i=1}^n (Y_i - \hat{Y}_i), \tag{3}$$

$$MSE = \frac{1}{n} \sum_{i=1}^n (Y_i - \hat{Y}_i)^2, \tag{4}$$

$$RMSE = \sqrt{\frac{1}{n} \sum_{i=1}^n (Y_i - \hat{Y}_i)^2}, \tag{5}$$

where \bar{Y} is mean observed data, n is number of data points, Y_i is observed values and \hat{Y}_i is predicted values.

3. Results and Discussion

All downstream flow velocities measurements for both numerical modelling and experimental study by SEGI (Clary *et al.*, 2020; Maitre *et al.*, 2013) were compared at $z/D = [2, 3, 4, 6, 8, 12]$, i.e., z is the distance from the cylindrical object along the length of the domain and D is the diameter of cylindrical object. Note that 2D, 3D etc here refer to the downstream distance from the cylindrical object. For example, 2D corresponds to $2 \times 5\text{m} = 10\text{m}$ behind the cylinder. Where velocities are compared between numerical and experimental methods, the velocities

are normalised by averaging the inflow velocity for $0.0 \leq y/D \leq 3.0$: 1.0 m/s for both approaches where y is the distance from the cylindrical object along with the depth of domain. The chosen flow velocity was a compromise between Malaysia’s average tidal stream velocity and the average minimum cut-in speed for tidal stream devices to generate electricity. Numerical simulation results in terms of the generated contour plots of the fluid flow interaction for cylindrical object in different type of turbulence models are shown in Fig. 8 while the extracted experimental data for each downstream distances (i.e. z/D) are illustrated in Fig. 9.

Numerical data points from each RANS turbulence models were extracted from Ansys Fluent across $0.0 \leq y/D \leq 3.0$ at $z/D = [2, 3, 4, 6, 8, 12]$ behind the cylindrical object. These set of data points were then compared with the extracted experimental data as shown in Fig. 9. The comparison of velocity profiles between published experimental data and this numerical study are illustrated in Fig. 10. From Fig. 10, it can be observed that the plotted data from various turbulence models generally exhibits a similar velocity profile as the experimental data across the extracted positions. Nonetheless, large centreline velocity deviations are apparent in the near wake, which is expected and will be discussed in the following section.

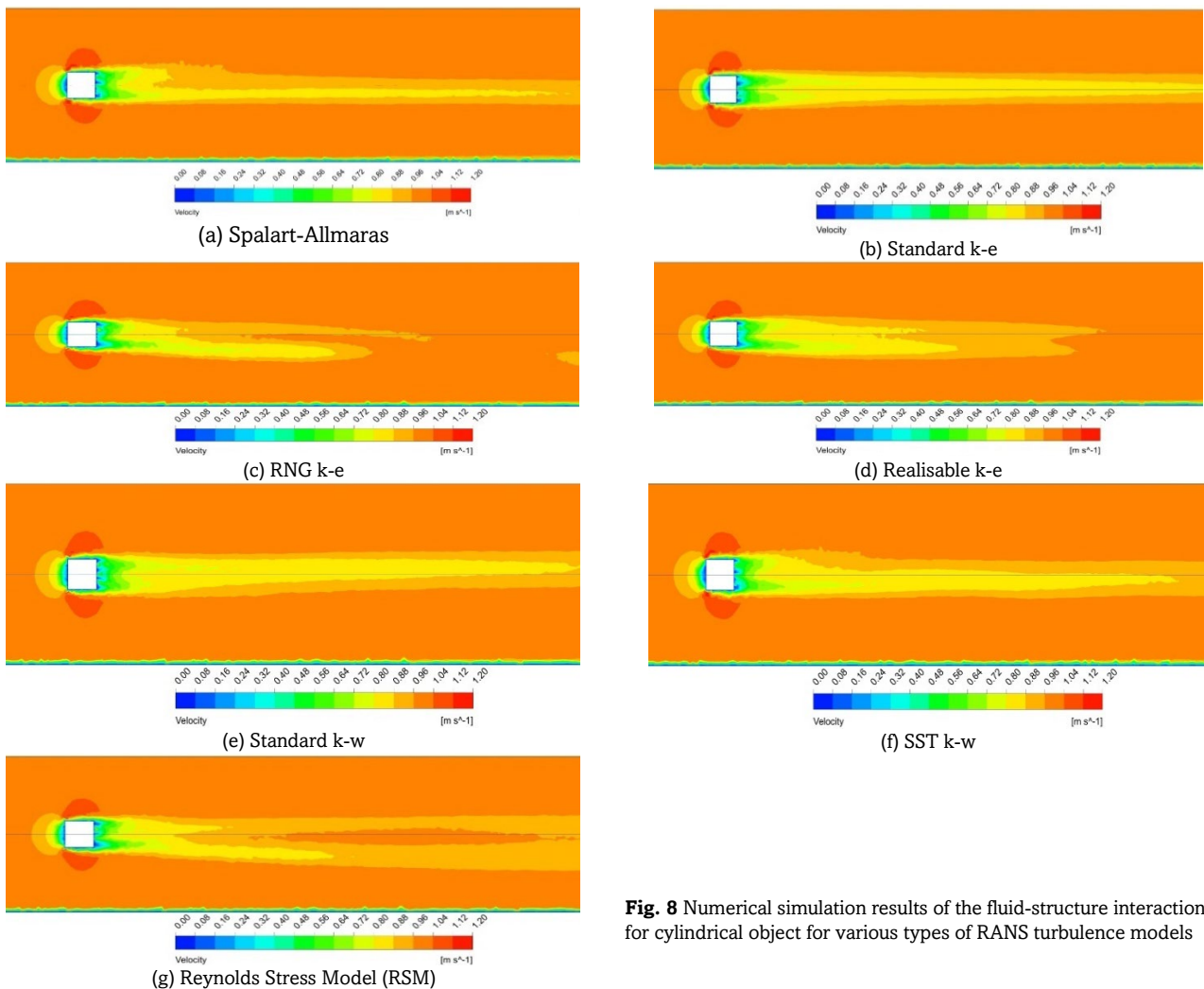


Fig. 8 Numerical simulation results of the fluid-structure interaction for cylindrical object for various types of RANS turbulence models

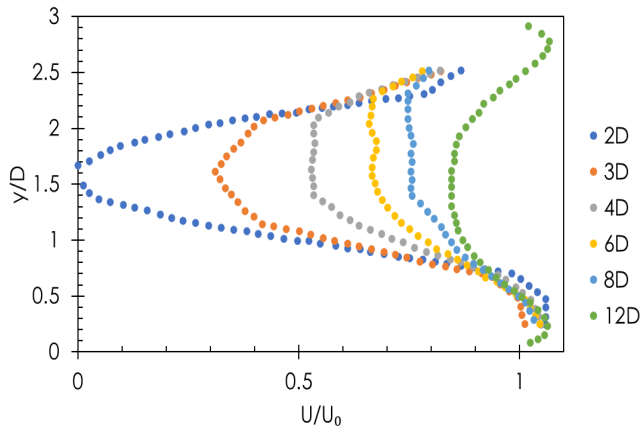


Fig. 9 Extracted velocity profile data from published study by Clary *et al.* (2020) at various downstream positions z/d of cylindrical object

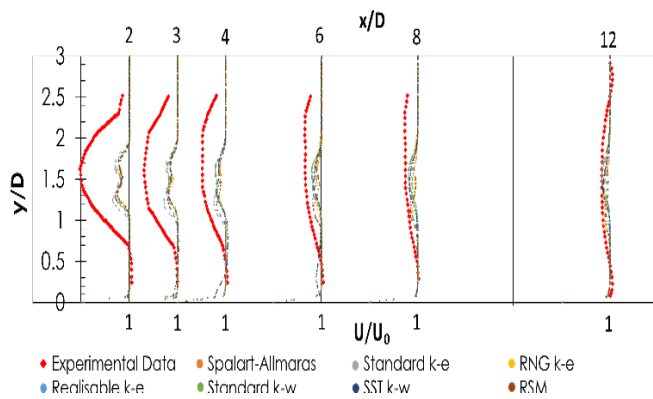
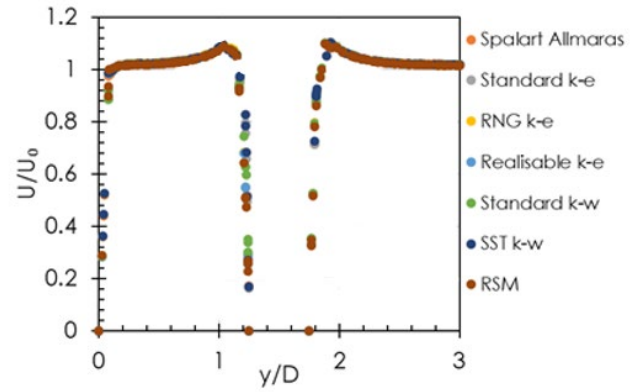


Fig. 10 Comparison of velocity profiles (experimental and simulated models) across y/D (depth) at various downstream positions behind the cylindrical object

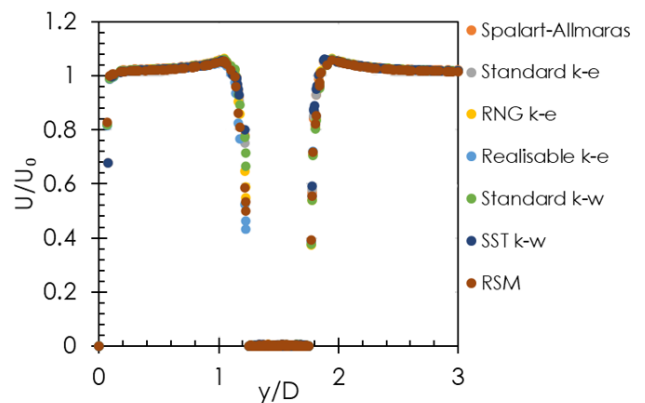
3.1 Immediate Vicinity Behind Cylinder

The velocity profile in the vicinity behind cylindrical object for different types of turbulence models used in the numerical simulation are plotted and displayed in Fig. 11. Velocities change downstream of the inlet due to the fact that the boundary layer has formed. This leads to significantly reduced streamwise velocities at $y/D < 0.5$, marginally greater streamwise velocities at $0.5 < y/D < 1.0$ and moderately decreased streamwise velocities at $y/D > 2.0$. However, the velocities at $1.0 < y/D < 2.0$ are significantly reduced when coming closer to the centreline and they are slightly reaching zero values. This is predominantly because of the presence of VATT at the centre $y/D = 1.5$ and dispersion of turbulent kinetic energy at downstream of a source, as stated in (ANSYS, 2011; ANSYS CFX-Solver, 2006; Harrison *et al.*, 2010).

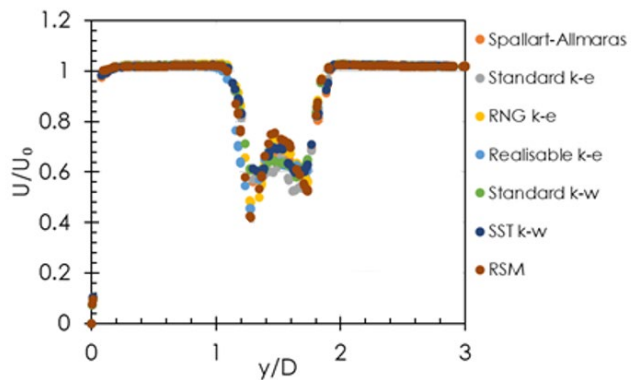
A velocity dip at the free surface is not represented. Stream velocity is predicted to reduce as it approaches the free surface. Secondary currents create this velocity dip phenomena, which is restricted to small channels (breadth less than five times depth) (Harrison *et al.*, 2010; Ng *et al.*, 2021). These phenomena are apparent in the scientific (i.e., experimental) results albeit not applicable in the numerical simulation. This is owing to the constraints of the RANS approach in simulating secondary currents.



(a) 0D downstream for RANS turbulence models



(b) 0.5D downstream for RANS turbulence models



(c) 1D downstream for RANS turbulence models

Fig. 11 Comparison of velocity profiles between numerical and experimental data at 0D, 0.5D, and 1D downstream of cylindrical object

The downstream wake development is also influenced by the inlet settings. These disagreements are expected to have implications on the downstream wake distribution in two behaviours. Firstly, the rate of recovery is reliant on the ambient turbulence intensity, therefore if the simulated turbulence intensity is smaller, the wake may recover more slowly (Harrison *et al.*, 2010; Myers & Bahaj, 2010). Secondly, acceleration of streamwise flows above the turbine is anticipated due to the obstruction effects, although these obstruction effects will be alleviated to a certain point by the existence of the free surface. For examples, the vorticity in the near-wake region of Spalart-Allmaras is governing by strain rate while the standard $k-\epsilon$ accounts for the anisotropy of the dissipation and the reduced mixing length due to the high strain rates present in the near-wake region. Because the free-surface

velocity effects are simulated differently than the experiments, it is expected that velocities in the upper half of the surrounding water will be greater in the wake zone than recorded.

3.2 Near-Wake Region

The downstream threshold of the near-wake region, as explained in Section 2.4, is the point where the wake edge shear layers combine at the wake centre-line, which commonly takes place at a region ranging between 2D and 6D downstream distance from the cylindrical object. The flow characteristics of cylindrical object dominate the near-wake: low pressure, stagnation and cylinder-induced turbulence. Because of the reasons stated in Section 2.4, substantial near wake agreement is not anticipated. However, a good understanding of the near-wake region is crucial because it produces the preliminary parameters for the far-wake turbulence. The velocities at the near-wake region for different types of turbulence models used in numerical simulation and experiment can be illustrated in Fig. 12.

Fig. 12 illustrates velocity profiles at 2D, 3D, 4D and 6D downstream distance from the cylindrical object along the centre-line. For all cases of downstream distances, region with the greatest velocity gradients (i.e., both below and above the centre-line) is the moment of shear layers occurrence at the wake edge. As the wake interacts with the free moving fluids, strong turbulence intensities are detected in this shear layer. As the resistance of cylindrical object (rotor) rises, increasing number of streamwise flow disperses around the rotor instead of going through it. As it advances towards the edges of cylindrical object, this transverse flow loses energy due to fluid viscosity. Concurrently, the velocity of water circulation which travels through the cylindrical object will decrease, and the dynamic pressure behind the cylinder will also be reduced and the flow becomes progressively stagnant.

The cylindrical object in numerical simulation is not a source of turbulence induced at downstream region, as mentioned in limiting factor 1 of Section 2.4. However, cylindrical object in the experiment accomplishes stream-wise momentum extraction by converting it to small-scale turbulence. It is stated in Section 2.4 that cylinder-induced turbulence will primarily disperse within the near-wake region. It is hypothesised that the cylinder-induced turbulence in the experiment entrains energy, driving the wake edge shear layer to grow more quickly and resulting in a shorter near wake area. Furthermore, in the model, the resistance coefficient imposed to the cylindrical item is isotropic; however, the resistance of a porous cylindrical object may not be isotropic, resulting in differing near-wake characteristics.

The difference between predicted and observed values were computed using Mean Absolute Error (MEA), Mean Square Error (MSE) and Root Mean Square Error (RMSE) where the statistical values are illustrated in Table 11. Table 11 demonstrates that the statistical error of the velocity profile decreases as it gets further away from the cylindrical object in the near-wake region. Based on Table 11, the spike of each RANS turbulence models is moving towards the centre with increasing downstream distance from 2D to 6D. The statistical error values are also decreasing in this trend.

At 2D downstream, the Standard $k-\epsilon$ model has the lowest MEA, MSE and RMSE values (0.4509, 0.3211 and 0.5666), while Realisable $k-\epsilon$ model have the lowest statistical errors at 3D downstream (0.3384, 0.1616 and 0.4020). At the same 3D downstream, Standard $k-\epsilon$ model exhibits the second lowest MEA, MSE and RMSE values (0.3424, 0.1621 and 0.4026), which is closer to the Realisable $k-\epsilon$ model. Increasing downstream distance to 4D, Realisable $k-\epsilon$ model still can accurately predict

the velocity profile of cylindrical objects (with errors of MEA = 0.2928, MSE = 0.1691 and RMSE = 0.4113) compared to six (6) other RANS turbulence models.

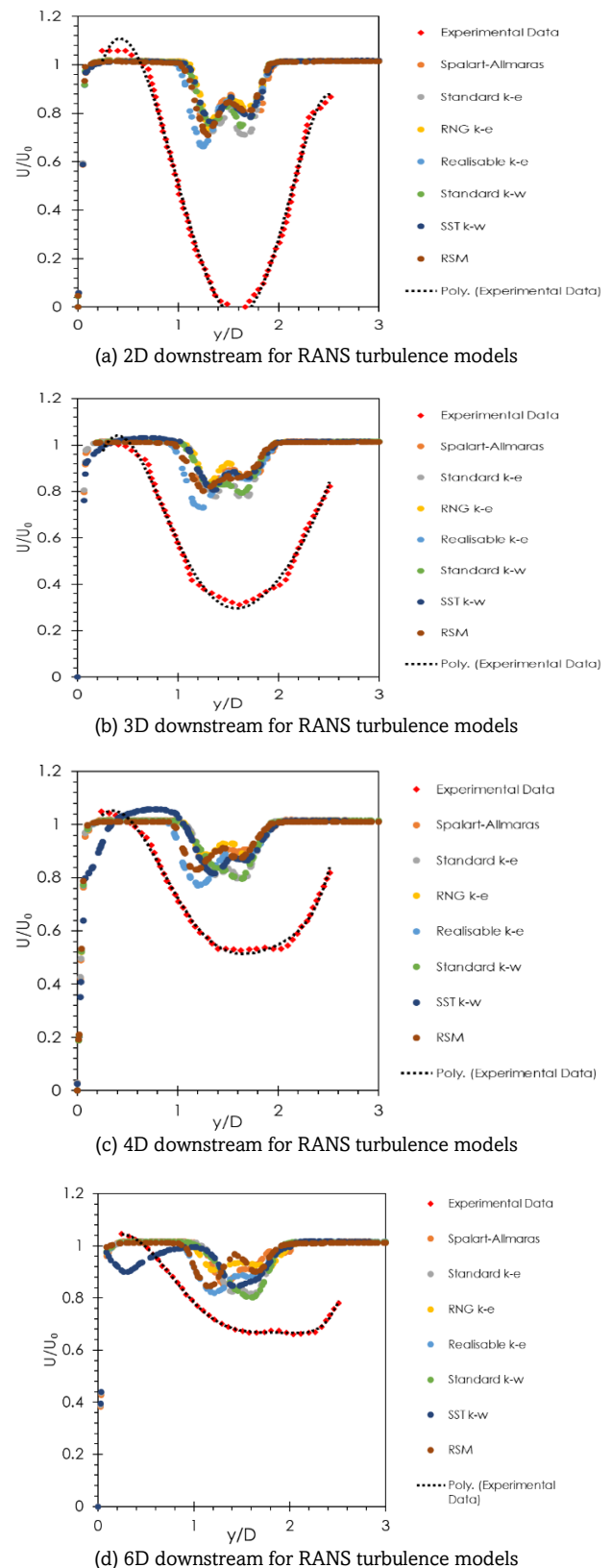


Fig. 12 Comparison of normalised velocities between numerical and experimental data at 2D, 3D, 4D and 6D downstream of cylindrical object

Table 11

Computed errors for 2D, 3D, 4D and 6D downstream for each RANS turbulence models

2D DOWNSTREAM			
Turbulence Models	Errors		
	MEA	MSE	RMSE
Spalart-Allmaras	0.4591	0.3344	0.5783
Standard k-ε	0.4509	0.3211	0.5666
RNG k-ε	0.4717	0.3617	0.6014
Realizable k-ε	0.4524	0.3381	0.5815
Standard k-ω	0.4646	0.3505	0.5921
SST k-ω	0.4613	0.3366	0.5802
RSM	0.4624	0.3493	0.5911

3D DOWNSTREAM			
Turbulence Models	Errors		
	MEA	MSE	RMSE
Spalart-Allmaras	0.3494	0.1694	0.4116
Standard k-ε	0.3424	0.1621	0.4026
RNG k-ε	0.3599	0.1806	0.4249
Realizable k-ε	0.3384	0.1616	0.4020
Standard k-ω	0.3515	0.1714	0.4140
SST k-ω	0.3492	0.1700	0.4123
RSM	0.3508	0.1720	0.4147

4D DOWNSTREAM			
Turbulence Models	Errors		
	MEA	MSE	RMSE
Spalart-Allmaras	0.3223	0.2027	0.4502
Standard k-ε	0.3154	0.1983	0.4454
RNG k-ε	0.3175	0.1822	0.4269
Realizable k-ε	0.2928	0.1691	0.4113
Standard k-ω	0.3056	0.1742	0.4173
SST k-ω	0.3338	0.2037	0.4513
RSM	0.3053	0.1756	0.4191

6D DOWNSTREAM			
Turbulence Models	Errors		
	MEA	MSE	RMSE
Spalart-Allmaras	0.2549	0.1236	0.3516
Standard k-ε	0.2441	0.1194	0.3455
RNG k-ε	0.2595	0.1313	0.3624
Realizable k-ε	0.2448	0.1264	0.3555
Standard k-ω	0.2503	0.1281	0.3580
SST k-ω	0.2552	0.1217	0.3489
RSM	0.2532	0.1304	0.3612

However, there are three models that able to accurately forecast the near-wake turbulences at 6D downstream. These models are Spalart-Allmaras (with errors of MEA = 0.2549, MSE = 0.1236 and RMSE = 0.3516), Standard k-ε (with errors of MEA = 0.2441, MSE = 0.1194 and RMSE = 0.3455) and SST k-ω (with errors of MEA = 0.2552, MSE = 0.1217 and RMSE = 0.3489). Thus, Standard k-ε is the most suitable model to be used for numerical simulation of cylindrical object at near-wake region due to its low statistical errors.

3.3 Far-Wake Region

Both simulation model and experimental results exhibit a similar pattern, particularly the rate of far-wake recovery. Fig. 13 illustrates that the centre-line wake velocity recovery follows a similar pattern in both models and experimental procedures when the shear layers have merged within the far-wake region. However, the far-wake values (velocity profile) in the experiment are greater than the results obtained from the numerical simulation of RANS turbulence models. The velocities at the far-wake region for different type of turbulence models used in numerical simulation and experiment are illustrated in Fig. 13.

The discrepancy observed between simulated results and the experiment is caused by two major factors. Firstly, since the experiments have a longer near-wake, the far-wake recovery begins later. Secondly, the rate of far-wake recovery is determined by ambient turbulence levels (Harrison *et al.*, 2010; Myers & Bahaj, 2010). Consequently, the low ambient turbulence levels at the inflow of the experiment presented in Section 3 mean that the wake recovers more slowly in the experiment.

The agreement in velocities profiles behind the cylindrical object differ with the depth of domain (y/D). Both Fig. 13 (a) and (b) demonstrate that there is a good agreement for experimental and numerical velocity profiles at y/D < 1.5. Nevertheless, at 8D downstream, the velocity profile of RANS numerical simulation at y/D > 1.5 differs significantly from experimental results, with the predicted velocity of turbulence flow (numerical) becoming faster than experimental flow.

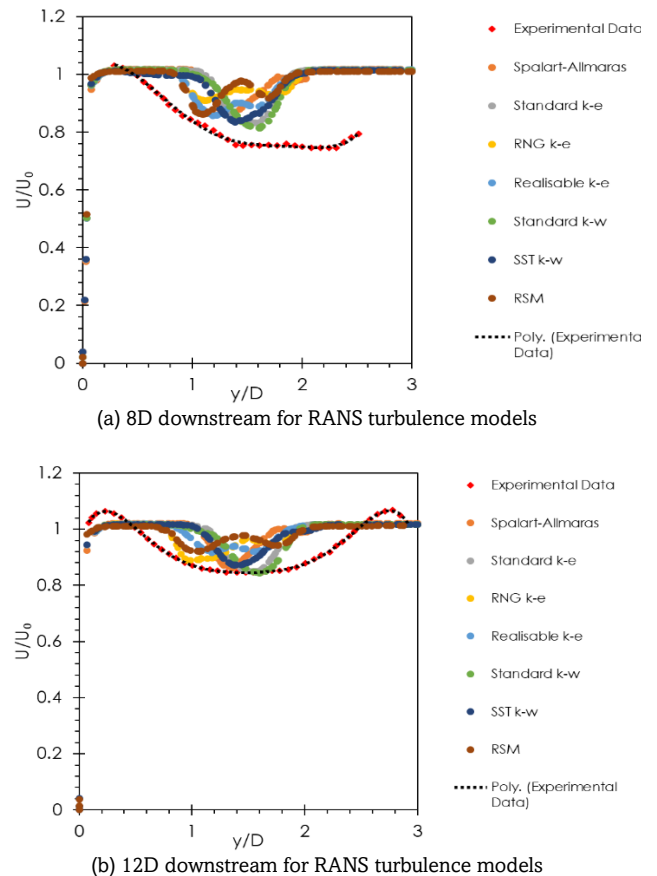


Fig. 13 Comparison of normalised velocities between numerical and experimental data at 8D and 12D downstream of cylindrical object

Table 12
Computed errors for 8D and 12D downstream for each RANS turbulence models

8D DOWNSTREAM			
Turbulence Models	Errors		
	MEA	MSE	RMSE
Spalart-Allmaras	0.1736	0.0542	0.2327
Standard k-ε	0.1678	0.0529	0.2299
RNG k-ε	0.1635	0.0465	0.2156
Realizable k-ε	0.1545	0.0446	0.2112
Standard k-ω	0.1550	0.0447	0.2115
SST k-ω	0.1624	0.0513	0.2265
RSM	0.1610	0.0468	0.2163

12D DOWNSTREAM			
Turbulence Models	Errors		
	MEA	MSE	RMSE
Spalart-Allmaras	0.0898	0.0244	0.1561
Standard k-ε	0.0840	0.0237	0.1539
RNG k-ε	0.0808	0.0222	0.1489
Realizable k-ε	0.0882	0.0232	0.1522
Standard k-ω	0.0810	0.0226	0.1504
SST k-ω	0.0855	0.0234	0.1528
RSM	0.0873	0.0235	0.1535

Besides, this poor agreement at $y/D > 1.5$ is resulted from inaccurate prediction and estimation of reduction of flow velocity at the free surface, as previously stated in Section 3. In contrast, there is a good agreement between numerical and experimental results at $y/D > 1.5$ for velocity profile at 12D downstream. This suggests that both numerical and experimental have achieved a similar rate of wake recovery at 12D downstream and beyond.

As mentioned previously, the difference between predicted and observed values can be evaluated using (MEA), (MSE) and (RMSE) where the statistical values are reported in Table 12. Based on Table 12, it can be highlighted that the statistical error of the velocity profile decreases as the downstream distance from the cylindrical object increases in the far-wake region. At 8D downstream, Realizable k-ε and Standard k-ω models have the lowest statistical errors (MEA = 0.1545 & 0.1550, MSE = 0.0446 & 0.0447, and RMSE = 0.2112 & 0.2115) while Spalart-Allmaras Model has the highest errors of MEA = 0.1736, MSE = 0.0542 and RMSE = 0.2327. On the other hand, at 12D downstream, the majority of the models can accurately predict the velocity profile of cylindrical object. However, RNG model exhibits lowest statistical errors of MEA = 0.0808, MSE = 0.0222 and RMSE = 0.1489 while Spalart-Allmaras Model has the highest errors of MEA = 0.0898, MSE = 0.0244 and RMSE = 0.1561. Therefore, the majority of these models are suitable to be used for numerical simulation of the cylindrical object at the far-wake region due to their low statistical errors.

4. Conclusion

This paper provides statistical analysis of the wake propagation at near-wake and far-wake regions of different types of RANS turbulence closure models using numerical simulation. The results were validated against published experimental data to

fully understand the magnitude of errors involved for selected RANS turbulence models. A hypothetical cylindrical approach was employed to represent the VATT in the simulation. For the near-wake region, the RANS numerical simulation outputs did not exhibit a conforming pattern as the velocity profile obtained from the experimental results. The lowest and highest RMSE values calculated based on statistical analysis are 0.5666 and 0.6111 at $z/D = 2$, 0.4020 and 0.4252 at $z/D = 3$, 0.4113 and 0.4513 at $z/D = 4$, 0.3455 and 0.3892 at $z/D = 6$, 0.2112 and 0.2694 at $z/D = 8$, as well as 0.1489 and 0.2129 at $z/D = 12$. This is predominantly because the RANS turbulence closure models underpredicted the occurrence of near-wake turbulence at 2D to 6D downstream. However, both RANS numerical simulation and experimental results demonstrated a similar velocity profile pattern at the far-wake region (8D and 12D downstream), particularly the rate of far-wake recovery.

In general, the discrepancy observed, which was translated into statistical errors using MEA, MSE, and RMSE at the near-wake region was greater than at the far-wake region. Based on the study conducted on statistical errors of near-wake and far-wake regions using hypothetical cylindrical approach, the following conclusion are made:

- i. For near-wake region: The statistical errors (RMSE values) of Standard k-ε model at $z/D = [2, 3, 4, 6, 8, 12]$ are 0.5666, 0.4026, 0.4454, 0.3455, 0.2299 and 0.1539. The statistical error of the velocity profile increased as the downstream distance from the cylindrical object decreases in the near-wake region. Based on the statistical analysis conducted, it can be concluded that standard k-ε is the most suitable model to be used for numerical simulation of the cylindrical object at the near-wake region due to low errors computed at 2D (RMSE = 0.5666), 3D (RMSE = 0.4026), 4D (RMSE = 0.4454) and 6D (RMSE = 0.3455) downstream from cylindrical object.
- ii. For far-wake region: In contrast, the statistical error of the velocity profile was found to be decreasing as the downstream distance from the cylindrical object increased in the far-wake region. For example, of Realizable k-ε model, the statistical errors (RMSE values) at $z/D = [8, 12]$ are 0.2112 and 0.1522. The analysis demonstrated that the majority of these models were suitable to be used for numerical simulation using cylindrical object at the far-wake region due to their low statistical errors.
- iii. For subsequent work: An artificial turbulent source term will be added into the numerical simulation to improve the near-wake turbulence. Artificial turbulent source term will be applied in a shallow water environment of Malaysia, where the presence of a 5.0-meter diameter turbine will be simulated for both single and array configuration. This will be done to examine the improved hypothetical cylinder theory's accuracy in modelling a full-size tidal device.

Acknowledgments

The authors gratefully acknowledge the financial support received from the Ministry of Higher Education Malaysia through the Fundamental Research Grant Scheme for Research Acculturation of Early Career Researchers (FRGSRACER) RACER/1/2019/TK07/UNIMAP/1. Additionally, the authors are also thankful for the support received from Universiti Malaysia Perlis, specifically from the Research Management Centre (RMC).

Author Contributions: Wafiuddin Rahim.: conceptualization, methodology, formal analysis, writing-original draft, Anas Rahman.: supervision, resources, project administration, methodology, writing-review and editing, Ayu Rahman.: writing-review and editing, statistical analysis, validation, Izham Ismail.: supervision, project administration, Shukry Majid.; writing-review and editing, Nasrul Amin.; writing-review and editing. All authors have read and agreed to the published version of the manuscript.

Funding: This research was funded by Ministry of Higher Education Malaysia through the Fundamental Research Grant Scheme for Research Acculturation of Early Career Researchers (FRGS-RACER) - RACER/1/2019/TK07/UNIMAP/1.

Conflicts of Interest: The authors declare no conflict of interest.

References

- Abdul Rahman, A. (2018). Numerical modelling of full scale tidal turbines using the actuator disc approach. *Proceedings of the 3rd Asian Wave and Tidal Energy Conference (AWTEC2016), Singapore - Vol 1*, 172–180.
- Abdullah, C., Mad Kaidi, H., Sarip, S., & Shafie, N. (2021). Small scale standalone solar and tidal hybrid power system in isolated area. *Renewable Energy Focus*, 39(00), 59–71. <https://doi.org/10.1016/j.ref.2021.07.010>
- Afgan, I., McNaughton, J., Rolfo, S., Apsley, D. D., Stallard, T., & Stansby, P. (2013). Turbulent flow and loading on a tidal stream turbine by LES and RANS. *International Journal of Heat and Fluid Flow*, 43, 96–108. <https://doi.org/10.1016/j.ijheatfluidflow.2013.03.010>
- ANSYS. (2011). *ANSYS CFD-Solver Theory Guide. Release 14.0. 15317*(November), 724–746. http://www1.ansys.com/customer/content/documentation/140/cfx_thry.pdf
- ANSYS. (2014). ANSYS - Turbulence Modelling and the Law of the Wall: Tutorial. *ANSYS User Manual*, 1–48.
- ANSYS. (2006). ANSYS CFX-Solver Theory Guide. *Release 11.0 (December)*, www.ansys.com/academic/learning-resources
- Bakri, A. (2020). *Numerical Assessment of Vertical Axis Marine Current Turbines Performances in Shallow Water : A Case Study for Malaysia*. Universiti Malaysia Perlis.
- Batten, W. M. J., Harrison, M. E., & Bahaj, A. S. (2013). Accuracy of the actuator disc-RANS approach for predicting the performance and wake of tidal turbines. *Philosophical Transactions of the Royal Society A: Mathematical, Physical and Engineering Sciences*, 371(1985). <https://doi.org/10.1098/rsta.2012.0293>
- Behrouzi, F., Maimun, A., Nakisa, M., Hanafi, M., & Jaswar. (2014). An innovative vertical axis current turbine design for low current speed. *Jurnal Teknologi (Sciences and Engineering)*, 66(2), 177–182. <https://doi.org/10.11113/jt.v66.2515>
- Blackmore, T., Batten, W. M. J., Harrison, M. E., & Bahaj, A. S. (2011). The Sensitivity of Actuator-Disc RANS Simulations to Turbulence Length Scale Assumptions. *Conference: 9th European Wave and Tidal Energy Conference, SouthamptonAt: Southampton, UK*.
- Bonar, P. A. J., Schnabl, A. M., Lee, W. K., & Adcock, T. A. A. (2018). Assessment of the Malaysian tidal stream energy resource using an upper bound approach. *Journal of Ocean Engineering and Marine Energy*, 4(2), 99–109. <https://doi.org/10.1007/s40722-018-0110-5>
- Cetina-Quiñones, A. J., López López, J., Ricalde-Cab, L., El Mekaoui, A., San-Pedro, L., & Bassam, A. (2021). Experimental evaluation of an indirect type solar dryer for agricultural use in rural communities: Relative humidity comparative study under winter season in tropical climate with sensible heat storage material. *Solar Energy*, 224(May), 58–75. <https://doi.org/10.1016/j.solener.2021.05.040>
- Ching, H. O. E. B. (2019). The Influence of Tidal Turbine In Array Configuration on The Wakw Formation For Shallow Water. In *School of Mechatronic Engineering* (Issue 161110607).
- Clary, V., Oudart, T., Larrourdé, P., Sommeria, J., & Maître, T. (2020). An optimally-controlled RANS Actuator force model for efficient computations of tidal turbine arrays. *Ocean Engineering*, 212(October 2019), 107677. <https://doi.org/10.1016/j.oceaneng.2020.107677>
- Ding, P., Wang, S., & Chen, K. (2020). Chinese Journal of Chemical Engineering Numerical study on turbulent mixed convection in a vertical plane channel using hybrid RANS / LES and LES models ☆. *Chinese Journal of Chemical Engineering*, 28(1), 1–8. <https://doi.org/10.1016/j.cjche.2019.04.007>
- Economic Planning Unit. (2015). *Rancangan Malaysia Kesebelas (Eleventh Malaysia Plan)* : 2016-2020. <http://rmk11.epu.gov.my/book/eng/Elevent-Malaysia-Plan/RMKe-11 Book.pdf>
- Elbatran, A. H. A., Yaakob, O. B., Ahmed, Y. M., & Abdullah, F. B. (2016). Augmented diffuser for horizontal axis marine current turbine. *International Journal of Power Electronics and Drive Systems*, 7(1), 235–245. <https://doi.org/10.11591/ijpeds.v7.i1.pp235-245>
- Elbatran, A. H., Yaakob, O. B., Ahmed, Y. M., & Shehata, A. S. (2018). Numerical and experimental investigations on efficient design and performance of hydrokinetic Banki cross flow turbine for rural areas. *Ocean Engineering*, 159(December 2017), 437–456. <https://doi.org/10.1016/j.oceaneng.2018.04.042>
- Garces, L. R., Stobutzki, I., Alias, M., Campos, W., Koongchai, N., Lachica-Alino, L., Mustafa, G., Nurhakim, S., Srinath, M., & Silvestre, G. (2006). Spatial structure of demersal fish assemblages in South and Southeast Asia and implications for fisheries management. *Fisheries Research*, 78(2–3), 143–157. <https://doi.org/10.1016/j.fishres.2006.02.005>
- Ghazvinei, P. T., Darvishi, H. H., & Bhatia, A. (2018). Sustainable power generation by tidal current turbine in straits of Malacca. *MATEC Web of Conferences*, 198. <https://doi.org/10.1051/mateconf/201819804004>
- Harrison, M. E., Batten, W. M. J., Myers, L. E., & Bahaj, A. S. (2010). Comparison between CFD simulations and experiments for predicting the far wake of horizontal axis tidal turbines. *IET Renewable Power Generation*, 4(6), 613–627. <https://doi.org/10.1049/iet-rpg.2009.0193>
- Hassanli, S. (2019). *Flow enhancement in and around buildings for wind energy harvesting. May*.
- Hassanzadeh, R., Yaakob, O. bin, Taheri, M. M., Hosseinzadeh, M., & Ahmed, Y. M. (2018). An innovative configuration for new marine current turbine. *Renewable Energy*, 120, 413–422. <https://doi.org/10.1016/j.renene.2017.11.095>
- Hoe, B. C. (2019). The Influence of Tidal Turbine In Array Configuration on The Wake Formation For Shallow Water. *School of Mechatronic Engineering*.
- Husain, M. K. A., Zaki, N. I. M., Husin, S. M. C., Mukhlas, N. A., Ahmad, S. Z. A. S., Husain, N. A., & Rashidi, A. H. M. (2019). Integrated tidal marine turbine for power generation with coastal erosion breakwater. *International Journal of Civil Engineering and Technology*, 10(2), 1277–1293. <http://www.iaeme.com/ijciect/issues.asp?JType=IJCIET&VTy pe=10&IType=2>
- Johnson, B., Francis, J., Howe, J., & Whitty, J. (2014). Computational Actuator Disc Models for Wind and Tidal Applications. *Journal of Renewable Energy*, 2014, 1–10. <https://doi.org/10.1155/2014/172461>
- Jump, E., Macleod, A., & Wills, T. (2020). Review of tidal turbine wake modelling methods—state of the art. *International Marine Energy Journal*, 3(2), 91–100. <https://doi.org/10.36688/imej.3.91-100>
- Kai, L. Y., Sarip, S., Kaidi, H. M., Ardila-Rey, J. A., Samsuddin, N. M., Muhtazaruddin, M. N., Muhammad-Sukki, F., & Aziz, S. A. (2021). Current Status and Possible Future Applications of Marine Current Energy Devices in Malaysia: A Review. *IEEE Access*, 9, 86869–86888. <https://doi.org/10.1109/ACCESS.2021.3088761>
- Lafleur, C., Truelove, W. AL, Cousineau, J., Hiles, C. E., Buckham, B., & Crawford, C. (2020). A screening method to quantify the economic viability of off-grid in-stream tidal energy deployment. *Renewable Energy*, 159, 610–622. <https://doi.org/10.1016/j.renene.2020.05.102>
- Lavaroni, L., Watson, S. J., Cook, M. J., & Dubal, M. R. (2014). A comparison of actuator disc and BEM models in CFD simulations for the prediction of offshore wake losses. *Journal of Physics: Conference Series*, 524(1). <https://doi.org/10.1088/1742-6596/524/1/012148>
- Lee, K. S., & Seng, L. Y. (2009). Simulation Studies on the Electrical

- Power Potential Harnessed by Tidal Current Turbines. *Journal of Energy and Environment*, 1, 18–23.
- Lim, Y. S., & Koh, S. L. (2010). Analytical assessments on the potential of harnessing tidal currents for electricity generation in Malaysia. *Renewable Energy*, 35(5), 1024–1032. <https://doi.org/10.1016/j.renene.2009.10.016>
- Maganga, F., Germain, G., King, J., Pinon, G., & Rivoalen, E. (2010). Institution of Engineering and Technology. *Archimer*, 4(6), 498–509.
- Maitre, T., Amet, E., & Pellone, C. (2013). Modeling of the flow in a Darrieus water turbine: Wall grid refinement analysis and comparison with experiments. *Renewable Energy*, 51, 497–512. <https://doi.org/10.1016/j.renene.2012.09.030>
- Mason-jones, A., Doherty, D. M. O., Morris, C. E., Doherty, T. O., Byrne, C. B., Prickett, P. W., Grosvenor, R. I., Owen, I., Tedds, S., & Poole, R. J. (2012). Non-dimensional scaling of tidal stream turbines. *Energy*, 44(1), 820–829. <https://doi.org/10.1016/j.energy.2012.05.010>
- Matus, B. I. (2016). *Aerodynamic Analysis and Rapid Prototyping of a Spiral Wind Turbine*. Kun Shan University of Science and Technology.
- Mohd Chachuli, F. S., Mat, S., Ludin, N. A., & Sopian, K. (2021). Performance evaluation of renewable energy R&D activities in Malaysia. *Renewable Energy*, 163, 544–560. <https://doi.org/10.1016/j.renene.2020.08.160>
- Myers, L. E., & Bahaj, A. S. (2010). Experimental analysis of the flow field around horizontal axis tidal turbines by use of scale mesh disk rotor simulators. *Ocean Engineering*, 37(2–3), 218–227. <https://doi.org/10.1016/j.oceaneng.2009.11.004>
- Ng, H. C. H., Collignon, E., Poole, R. J., & Dennis, D. J. C. (2021). Energetic motions in turbulent partially filled pipe flow. *Physics of Fluids*, 33(2). <https://doi.org/10.1063/5.0031639>
- Petinrin, J. O., & Shaaban, M. (2015). Renewable energy for continuous energy sustainability in Malaysia. *Renewable and Sustainable Energy Reviews*, 50, 967–981. <https://doi.org/10.1016/j.rser.2015.04.146>
- Rahman, A., Ibrahim, I., & Rahman, M. T. A. (2019). Assessment of the Malaysian Tidal Stream Energy Resources. *IOP Conference Series: Materials Science and Engineering*, 670(1). <https://doi.org/10.1088/1757-899X/670/1/012025>
- Ren, H., Zhang, X., Kang, S., & Liang, S. (2019). Actuator disc approach of wind turbine wake simulation considering balance of turbulence kinetic energy. *Energies*, 12(1). <https://doi.org/10.3390/en12010016>
- Sakmani, A. S., Lam, W. H., Hashim, R., & Chong, H. Y. (2013). Site selection for tidal turbine installation in the Strait of Malacca. *Renewable and Sustainable Energy Reviews*, 21, 590–602. <https://doi.org/10.1016/j.rser.2012.12.050>
- Salem, A., Souf, M., & Maimun, A. D. I. (2015). Low speed vertical axis current turbine for electrification of remote areas in Malaysia. *Recent Advances in Renewable Energy Sources*, 75–82.
- Salunkhe, S., Fajri, O. El, Bhushan, S., Thompson, D., O'Doherty, D., O'Doherty, T., & Mason-Jones, A. (2019). Validation of Tidal Stream Turbine Wake Predictions and Analysis of Wake Recovery Mechanism. *Journal of Marine Science and Engineering*, 7(10). <https://doi.org/10.3390/jmse7100362>
- Samo, K. A., Samo, I. A., Siyal, Z. A., & Rigit, A. R. H. (2020). Determination of Potential Tidal Power Sites at East Malaysia. *Engineering, Technology & Applied Science Research*, 10(4), 6047–6051. <https://doi.org/10.48084/etasr.3674>
- Shen, W. Z. (2002). Numerical Modeling of Wind. *Journal of Fluid Engineering*, 124(June), 393–399. <https://doi.org/10.1115/1.1471361>
- Shur, M. L., Spalart, P. R., Kh, M., & Travin, A. K. (2008). International Journal of Heat and Fluid Flow A hybrid RANS-LES approach with delayed-DES and wall-modelled LES capabilities. *International Journal of Heat and Fluid Flow*, 29(6), 406–417. <https://doi.org/10.1016/j.ijheatfluidflow.2008.07.001>
- Tedds, S. C., Owen, I., & Poole, R. J. (2014). Near-wake characteristics of a model horizontal axis tidal stream turbine. *Renewable Energy*, 63, 222–235. <https://doi.org/10.1016/j.renene.2013.09.011>
- V M M G Costa Gomes, J M L M Palma, & A Silva Lopes. (2014). Improving actuator disk wake model. *Journal of Physics: Conference Series* 524. <https://doi.org/10.1088/1742-6596/524/1/012170>
- Vermeer, L. J., S, J. N., & Crespo, A. (2003). Wind turbine wake aerodynamics. *Progress in Aerospace Sciences*, 39, 467–510. [https://doi.org/10.1016/S0376-0421\(03\)00078-2](https://doi.org/10.1016/S0376-0421(03)00078-2)
- Vinod, A., Han, C., & Banerjee, A. (2021). Tidal turbine performance and near-wake characteristics in a sheared turbulent in flow. *Renewable Energy*, 175, 840–852. <https://doi.org/10.1016/j.renene.2021.05.026>
- Wang, Y., & Liu, Z. (2021). Proposal of novel analytical wake model and GPU-accelerated array optimization method for oscillating wave surge energy converter. *Renewable Energy*, 179, 563–583. <https://doi.org/10.1016/j.renene.2021.07.054>
- Yaakob, O. B., Suprayogi, D. T., Abdul Ghani, M. P., & Tawi, K. B. (2013). Experimental studies on savonius-type vertical axis turbine for low marine current velocity. *International Journal of Engineering, Transactions A: Basics*, 26(1), 91–98. <https://doi.org/10.5829/idosi.ije.2013.26.01a.12>
- Yaakob, O. B., Yasser, M., Bin Mazlan, M. N., Jaafar, K. E., & Raja Muda, R. M. (2013). Model testing of an ocean wave energy system for Malaysian sea. *World Applied Sciences Journal*, 22(5), 667–671. <https://doi.org/10.5829/idosi.wasj.2013.22.05.2848>
- Yaakob, O., M. Yusuf, M. A., Jamian, J. J., Baharudin, M. A., Kang, H. S., Shaharuddin, N. M. R., Hashim, F. E., Aspar, Z., Mustapa, M. A., Ismail, M. A., Abd Rahim, A. M., Bazli, M. S., Khaliddin, N., & Jupri, S. S. (2018). Combined ocean renewable energy system (CORES) for islandic area on Malaysian seas. *The Asian Wave and Tidal Energy Conference (AWTEC) 2018*.
- Yaakob, O., Rashid, T. A., & Mukti, M. (2006). Prospects for ocean energy in Malaysia. *International Conference on Energy and Environment 2006*, 2006(August), 1–7. http://www.uniten.edu.my/newhome/uploaded/coe/icee2006/proceedings/renewable_energy_technology/UNITEN_ICEE_2006_Prospects_for_Ocean_Energy_in_Malaysia.pdf
- Yang, Q., Li, H., Li, T., & Zhou, X. (2021). Wind farm layout optimization for levelized cost of energy minimization with combined analytical wake model and hybrid optimization strategy. *Energy Conversion and Management*, 248, 114778. <https://doi.org/10.1016/j.enconman.2021.114778>

